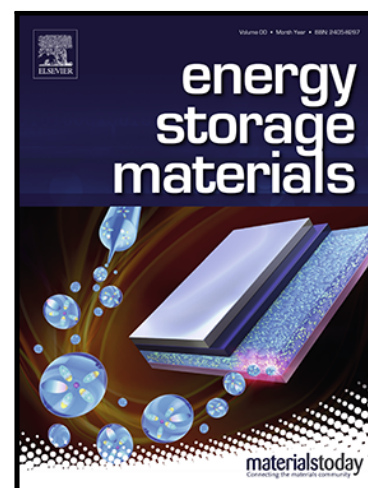


Journal Pre-proof

Enhanced electrochemical and environmental stability of black phosphorus-derived phosphorus composite anode for safe potassium-ion battery using amorphous zinc phosphate as a multi-functional additive

Shunping Ji , Yunshan Zheng , Kwan San Hui , Junfeng Li , Kaixi Wang , Chunyan Song , Huifang Xu , Shuo Wang , Chenyang Zha , Duc Anh Dinh , Zikang Tang , Zongping Shao , Kwun Nam Hui



PII: S2405-8297(23)00045-4
DOI: <https://doi.org/10.1016/j.ensm.2023.01.036>
Reference: ENSM 2666

To appear in: *Energy Storage Materials*

Received date: 9 September 2022
Revised date: 9 January 2023
Accepted date: 21 January 2023

Please cite this article as: Shunping Ji , Yunshan Zheng , Kwan San Hui , Junfeng Li , Kaixi Wang , Chunyan Song , Huifang Xu , Shuo Wang , Chenyang Zha , Duc Anh Dinh , Zikang Tang , Zongping Shao , Kwun Nam Hui , Enhanced electrochemical and environmental stability of black phosphorus-derived phosphorus composite anode for safe potassium-ion battery using amorphous zinc phosphate as a multi-functional additive, *Energy Storage Materials* (2023), doi: <https://doi.org/10.1016/j.ensm.2023.01.036>

This is a PDF file of an article that has undergone enhancements after acceptance, such as the addition of a cover page and metadata, and formatting for readability, but it is not yet the definitive version of record. This version will undergo additional copyediting, typesetting and review before it is published in its final form, but we are providing this version to give early visibility of the article. Please note that, during the production process, errors may be discovered which could affect the content, and all legal disclaimers that apply to the journal pertain.

© 2023 Published by Elsevier B.V.

Enhanced electrochemical and environmental stability of black phosphorus-derived phosphorus composite anode for safe potassium-ion battery using amorphous zinc phosphate as a multi-functional additive

Shunping Ji†, Yunshan Zheng†, Kwan San Hui, Junfeng Li, Kaixi Wang, Chunyan Song, Huifang Xu, Shuo Wang, Chenyang Zha, Duc Anh Dinh, Zikang Tang, Zongping Shao*, and Kwun Nam Hui**

S. P. Ji, Y. S. Zheng, J. F. Li, K. X. Wang, H. F. Xu, S. Wang, Prof. C.Y. Zha, Prof. Zikang Tang, Prof. K. N. Hui
Joint Key Laboratory of the Ministry of Education, Institute of Applied Physics and Materials Engineering, University of Macau, Avenida da Universidade, Taipa, Macau SAR, P.R. China
E-mail: bizhui@um.edu.mo

Prof. K. S. Hui
School of Engineering, Faculty of Science, University of East Anglia, Norwich, NR4 7TJ, United Kingdom
E-mail: k.hui@uea.ac.uk

C. Y. Song
Analysis and Testing Center, Shenzhen Technology University, Shenzhen 518118, China

Prof. D. A. Dinh
VKTech Research Center, NTT Hi-Tech Institute, Nguyen Tat Thanh University, Ho Chi Minh City 700000, Vietnam

Prof. Z. P. Shao
WA School of Mines: Minerals, Energy and Chemical Engineering (WASM-MECE), Curtin University, Perth, WA 6845, Australia
E-mail: zongping.shao@curtin.edu.au

Keywords: BP, amorphous phosphorus, amorphous zinc phosphate, PIB, electrode environmental stability.

Black phosphorus (BP) presents high theoretical capacity as potassium-ion battery (PIB) anode, while low ionic/electronic conductivity for bulk phase and high volume expansion and extremely sensitivity to humid environment for its nanomaterial hinder its practical applications. Here, we propose BP nanocomposites with amorphous zinc phosphate to tackle above problems. The amorphous zinc phosphate plays multifunctional roles in weakening the agglomeration of BP nanomaterials, reducing the volume expansion and improving the environmental stability of BP nanocomposite electrodes in humid air. The optimized

amorphous BP nanocomposite anode with 30wt% zinc phosphate, BP@C@ZPO(30), retains capacity of $369.0 \text{ mA h g}^{-1}$ after 500 cycles at 0.5 A g^{-1} in a noninflammable triethyl phosphate (TEP) electrolyte, and the volume expansion rate of the BP@C@ZPO(30) electrode is reduced to 47% compared with BP@C@ZPO(0) electrode of 100%. More attractively, the amorphous zinc phosphate improves the environmental stability of the nanocomposite electrode in humid air due to its features of strong and fast physical absorption to water. Consequently, the BP@C@ZPO(30) electrode delivers a reversible capacity of $629.2 \text{ mA h g}^{-1}$ (200 cycles at 0.2 A g^{-1}) even after exposing the electrode to humid air for two days. Such nanocompositing strategy may accelerate the practical application of phosphorus electrode.

Introduction

Potassium-ion batteries (PIBs) are regarded as strong competitors to replace lithium-ion batteries (LIBs) as the future energy storage devices due to their potential low cost and high power/energy density.^[1] Nevertheless, PIBs have more stringent requirements on the electrode materials due to the large ionic radius of potassium ions (1.38 \AA). For instance, routine graphite anode only forms KC_8 phase rather than KC_6 phase when used as PIB anode and leads to an unsatisfactory theoretical capacity of $279.0 \text{ mA h g}^{-1}$.^[2] Therefore, developing relatively high specific capacity of anodes is particularly critical to improving the energy density of PIBs for practical applications. Phosphorus, mainly referring to red phosphorus (RP) and black phosphorus (BP) allotropes, has received remarkable attention as anode of metal-ion batteries due to its high theoretical specific capacity, abundant reserve, and acceptable cost.^[3] In addition, phosphorus has high theoretical specific capacity of 2596, 1154, and 865 mA h g^{-1} on the basis of formed K_3P ,^[3a] K_4P_3 ,^[4] and KP ^[5] alloying phases, respectively, as the PIB anode.

BP shows higher electronic conductivity ($\sim 300 \text{ S m}^{-1}$), more stable structure, and higher safety during operation than RP.^[6] Despite these advantages, however, some problems still need to be solved prior to use, including 1) low ionic conductivity, the low K-ion diffusion coefficient, especially during the formation of K_3P phase, severely decreases the utilization of BP.^[3a] 2) Huge volume variation, the theoretical volume expansion rates of BP are over 300% and 600% when forming KP and K_3P phases, respectively, in PIBs.^[3a] Evidently, huge volume expansion of electrode considerably reduces the stability of solid electrolyte interphase (SEI).^[7] Thus far, many strategies have been adopted to improve the electrochemical performance of phosphorus materials in PIBs. Reducing the size of the active materials is an efficient strategy, which can shorten ionic/electronic diffusion length, increase the utilization rate of active materials, and then improve the specific capacity.^[8] Therefore, the strategy of embedding nano-sized phosphorus particles in the conductive carbon matrixes has been widely adopted to improve the conductivity and relieve volume expansion. These conductive carbon matrixes include nanofibers^[4, 9], nanotubes^[3b, 6b], nanorods,^[10] 2D graphene,^[11] and 3D carbon framework^[5, 12]. Although significant advances have been made using these means, the high cost and complicated preparing process are unsuitable for the large-scale production and application. Furthermore, nano-sized BP materials are sensitive to oxygen and water, which can rapidly degrade when exposed to humid environment.^[13] Therefore, enhancing the environmental stability of BP nanoparticles is also a key issue to extend its application and operational time and reduce the cost of transportation and storage.^[14]

Although a simple and low-cost ball milling method can improve the electrochemical performance of BP by forming BP nanocomposites with carbon materials due to the formation of chemical bonds between phosphorus and carbon, the obtained samples tend to form compact aggregations and cannot effectively solve the issue of volume expansion.^[15] Amorphous structure can tolerate larger volume variation than that of its crystalline state and

can also facilitate ion diffusion due to isotropy.^[16] Thus, in our recent research, we demonstrate that amorphous metal phosphides can be obtained by introducing zinc phosphate during the ball milling process after optimizing the synthesis conditions.^[17] Furthermore, the formed active/inactive composite when introducing inactive amorphous zinc phosphate component is more conducive to relieving volume expansion and improving ion conductivity of active materials.^[18] In addition, amorphous zinc phosphates have the property of rapid response to water.^[19] However, whether they can function as desiccants to resist moisture has not been studied. Finally, selecting a suitable electrolyte system to form a stable SEI also plays a significant role in the enhanced battery performance of phosphorus electrodes.^[20] Compared with the conventional EC/DEC electrolyte system, a noninflammable triethyl phosphate (TEP) electrolyte system shows enhanced cycling stability and improved safety in PIBs.^[21]

Therefore, on the basis of this research and analysis, the multifaceted problems of BP anode were considered comprehensively, and then the amorphous zinc phosphate (A-ZPO) as an additive was introduced into the BP to form amorphous BP nanocomposites. First, the A-ZPO acted as grinding aids to reduce the aggregation and regrowth of active materials during the dry ball milling process, which increases the dispersity of materials and leads to the size reduction and improvement of the utilization of active materials. Second, the addition of A-ZPO improved the ability of buffering volume expansion of the electrodes, and the volume expansion rate of the BP@C@ZPO(30) electrode was reduced to 47% relative to the 100% of the BP@C@ZPO(0) electrode. Third, using low-cost zinc phosphate can reduce the cost of electrode materials. Finally, and most interestingly, the introduction of A-ZPO improved the ability of the electrode to resist moisture by utilizing features of strong and fast physical absorption of nano-sized A-ZPO to water. Evidently, the A-ZPO showed a multi-function, and the optimized amorphous BP nanocomposite with 30wt% A-ZPO showed an optimized electrochemical performance when used as PIB anode. It delivered retained capacities of

369.0 mA h g⁻¹ (500 cycles at 0.5 A g⁻¹) and 629.2 mA h g⁻¹ after 200 cycles at 0.2 A g⁻¹ even after exposure of the electrode to humid air for two days in a nonflammable triethyl phosphate (TEP) electrolyte. We hope that such a low cost and effective strategy can accelerate the practical application of phosphorus anode for metal-ion batteries.

Results and discussion

To compare and analyze the safety of the prepared nanocomposites, red phosphorus (RP) and black phosphorus (BP) were first used to prepare their carbon-contained nanocomposites without adding zinc phosphate by dry ball milling method. A spontaneous combustion phenomenon for the prepared RP@C composite occurred when exposed to air, as shown in **Figure 1a**, due to the formation of flammable white phosphorus (WP) at the high temperature in the inert atmosphere.^[6c, 11c, 17] By contrast, the BP@C composite showed good stability when exposed to air, indicating no or little WP formed under the same preparation conditions. The results confirmed a better operational safety for BP than that of RP when preparing the phosphorus-based nanocomposites. Therefore, BP was selected as raw material to prepare the nanocomposites with amorphous zinc phosphate (A-ZPO). The BP composites with different mass fractions of A-ZPO were designed and prepared, and the obtained composites were labeled as BP@C@ZPO(0, 10, 20, 30, and 40) based on the mass fractions of A-ZPO added. Their TGA data are shown in Figure S1. The calculated mass fractions of phosphorus are close to their designed values except the BP@C@ZPO(0) sample due to the oxidation of phosphorus. The X-ray diffraction patterns of BP and its composites are shown in Figure 1b, the evident diffraction peaks assigned to BP (JCPDS No. 76-1957), such as (020), (021), (040), and (111), were detected for the pure BP materials, belonging to orthorhombic system and Cmca space group.^[22] However, the samples with carbon and A-ZPO showed weak or even disappeared BP diffraction peaks, suggesting that the crystalline BP transformed into the amorphous state when introducing carbon and A-ZPO. Meanwhile, the added zinc phosphate

also presented an amorphous state. The Raman spectrum of pure BP showed three characteristic peaks belonging to bulk BP at ~ 357 , ~ 429 , and ~ 459 cm^{-1} , corresponding to A_g^1 (out-of-plane mode), B_{2g} , and A_g^2 (in-plane mode) modes, respectively (Figure 1c).^[23] The Raman spectra showed no signals of BP for the other samples due to the amorphous state and the interference of added components (carbon and zinc phosphate).^[20b] In addition, the D band (~ 1335 cm^{-1}) and G band (~ 1590 cm^{-1}) belonging to carbon were detected in all the samples with Super P.^[24] XPS survey spectra confirmed all Zn, C, P, and O elements in the samples with zinc phosphate (Figure 1d). The fitted high-resolution XPS spectra are shown in Figure 1e, the C1s spectra of five samples presented sp^2 (C=C/C-C, ~ 284.1 eV) and sp^3 (C-C, ~ 285.0 eV) assigned to Super P, and a few carbon-based species with high valance states of the C-O (~ 286.4 eV) and C=O (~ 288.8 eV) bonds were also found due to the ineluctable oxidation or surface contamination.^[25] The O1s spectra showed that the P=O/C=O (~ 533.1 eV) and P-O⁻/C-O (~ 531.5 eV) bonds stemmed from the phosphorus oxide (P_xO_y), zinc phosphate, and carbon-based oxides. The P2p spectra confirmed the P-P bonds ($2p_{3/2}$: ~ 129.7 eV; $2p_{1/2}$: ~ 130.6 eV) of phosphorus and P=O/P-O⁻ bonds (133.4 – 134.1 eV) of P_xO_y and zinc phosphate in all five samples.^[26] Except for the BP@C@ZPO(0), Zn2p spectra ($2p_{3/2}$: ~ 1022.1 eV; $2p_{1/2}$: ~ 1045.2 eV) can be detected in all other samples due to the addition of zinc phosphate.

The high-resolution transmission electron microscopy (HRTEM) of pure BP, as shown in **Figure 2a** and **b**, indicated the interplanar spacings of 0.336 and 0.262 nm belonging to the crystal planes of (021) and (040) of BP, respectively. In addition, the corresponding Fast Fourier Transform (FFT) pattern confirmed the results (Figure 2c), which are consistent with the X-ray diffraction results. By comparison, no lattice fringe was observed in the BP@C@ZPO(30) sample (Figure 2d and e). Moreover, the selected area electron diffraction (SAED) pattern showed no diffraction spots and polycrystalline diffraction rings. This finding verifies that the amorphous structure is the same as that in the XRD results, indicating that the

addition of zinc phosphate reduced the crystallinity of BP (Figure 2f). A homogeneous distribution of P, Zn, C, P, and O elements was observed in the TEM elemental mappings for the BP@C@ZPO(30) sample, suggesting the formation of nanocomposite (Figure 2g). In addition, the TEM images and elemental mappings of BP@C@ZPO(10), BP@C@ZPO(20), and BP@C@ZPO(40) have also been analyzed, as shown in Figure S2, Figure S3 and Figure S4, all these samples also showed amorphous structure and homogeneous elemental distribution. However, reducing the size of particles will increase the specific surface energy and lead to the aggregation and regrowth of the nanocomposites during dry ball milling process.^[27] Evidently, aggregation phenomenon of prepared composites was also observed in this work, especially for the BP@C@ZPO(0) sample. As shown in Figure 2h, large number of large-sized BP@C aggregations were observed by scanning electron microscopy (SEM) even after 5 minutes of sonication in ethanol, indicating that compact aggregations were formed due to the high specific surface energy. However, loose aggregations were found in the BP@C@ZPO(20) sample due to the introduction of appropriate zinc phosphate (Figure 2i), and such unconsolidated agglomerations were easily broken up in the BP@C@ZPO(30) sample after the same treatment as BP@C@ZPO(0) sample (Figure 2j). The results suggest that the existence of zinc phosphate was against the compact agglomeration of BP particles, thereby facilitating the dispersibility and uniformity of active materials during electrode preparation. In addition, the particle size distributions of all five samples were also tested using dynamic light scattering method with a Zetasizer. All the samples were dispersed in water and tested three times for comparison. As shown in Figure 2k, the size distributions of five samples are mainly composed of two parts, micron-sized aggregations and nano-sized primary particles. The figure shows that the number of primary particles increased markedly with the increase in the content of zinc phosphate, and the statistical average particle size decreased from 776 nm to 477 nm with the increase in zinc phosphate from 0 wt% to 40 wt% (Figure 2l). The results are consistent with the SEM data and confirm that zinc phosphate

acted as a ball milling assistant to relieve the agglomeration based on the mechanism of decreasing the direct contact probability between the BP@C particles. The proposed schematic is shown in Figure 2m. Furthermore, the uniform size and distributions of the active materials on the electrode surface are beneficial to equilibrate the current distribution during the charging/discharging process of the electrode and to reduce the local side-reaction.^[28]

The prepared composites were exposed to the humid environment (relative humidity: 65%±5) to analyze the sensitivity to the humid environment. After three days, as shown in **Figure 3a**, the XPS results showed that all the BP@C@ZPO(0) and BP@C@ZPO(30) samples were oxidized to form phosphorus oxide (P_xO_y),^[13c] and only a small peak belonging to unoxidized phosphorus was detected for BP@C@ZPO(30) sample, indicating that the introduction of amorphous zinc phosphate could not protect the phosphorus from oxidation. However, when the fresh BP@C@ZPO(0) and BP@C@ZPO(30) electrodes were exposed to moist air, the BP@C@ZPO(0) electrode showed an evident hygroscopic phenomenon (Figure 3b i). Moreover, evident spots were observed on the electrode surface after drying the hygroscopic electrodes (Figure 3b ii), suggesting that some reactions occurred on the electrode surface. By contrast, no hygroscopic phenomenon was observed on the BP@C@ZPO(30) electrode surface under the same conditions (Figure 3biii). To determine the reaction mechanism of the hygroscopic electrodes, they were analyzed by XRD after placing in humid air for three days (relative humidity: 65%±5). The results showed that hydrated copper pyrophosphate ($Cu_2P_2O_7 \cdot 3H_2O$, JCPDS No. 51-0202) was formed (Figure 3c), and the compound was detected in all the electrodes with zinc phosphate content lower than 30 wt%. The diffraction peak intensity of copper pyrophosphate decreased with the increase in zinc phosphate content, and no diffraction peaks of copper pyrophosphate can be found in the BP@C@ZPO(30) and BP@C@ZPO(40) electrodes, indicating that the presence of zinc phosphate can inhibit the formation of this compound. In addition, the flower-like

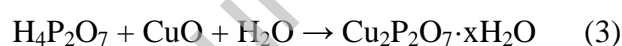
morphology of copper pyrophosphate was observed on the BP@C@ZPO(0) electrode surface (Figure 3d and e). Its corresponding EDS spectrum also confirmed the presence of copper pyrophosphate compound because the main O, Cu, and P elements were detected and the experimental value of atomic ratio of P/Cu is 1.00:0.95, which is same to the theoretical value (1:1) of copper pyrophosphate (Figure S5). Furthermore, with the increase in zinc phosphate, no large flower-shaped copper pyrophosphate was observed. Meanwhile, the proportion of copper pyrophosphate in the electrodes decreased (Figure S6). In particular, no copper pyrophosphate compound was found in the BP@C@ZPO(30) electrode surface (Figure 3f and g); this finding agrees well with the XRD results. Our analysis indicated that the addition of zinc phosphate did not inhibit the oxidation of phosphorus. Therefore, we directly used the easily hygroscopic P_2O_5 , representing the oxidized phosphorus formed on the surface of phosphorus particles, to analyze the enhanced anti-moisture ability of electrodes when introducing A-ZPO. The P_2O_5 and A-ZPO were mixed well in the glovebox before testing in the humid air (relative humidity: $65\% \pm 5$). As shown in Figure 3h, evident deliquescence phenomenon occurred when exposed to air at not more than 10 s for pure P_2O_5 . After 24 h, hydrated copper pyrophosphate ($Cu_2P_2O_7 \cdot 3H_2O$, JCPDS No. 51-0202), and anhydrous copper pyrophosphate ($Cu_2P_2O_7$, JCPDS No. 44-0182) were formed and observed on the edges of Cu current collector, as verified by the XRD analysis in Figure 3i. By contrast, pure amorphous zinc phosphate (A-ZPO) and the mixture of P_2O_5 and A-ZPO (mass ratio: $P_2O_5/A-ZPO = 3/7$) did not change significantly under the same conditions. The results showed that the presence of A-ZPO alleviates the deliquescence of the P_2O_5 . However, the addition of insufficient A-ZPO (mass ratio: $P_2O_5/A-ZPO = 5/5$) and crystalline zinc phosphate (C-ZPO) could not alleviate the deliquescence of P_2O_5 (Figure S7–9).

We further analyzed the mechanism (physical or chemical reactions) on the alleviation of the deliquescence of the electrode with A-ZPO by directly using pure zinc phosphate. First, the contact angle test showed that a droplet can be rapidly absorbed by the A-ZPO film in less

than 3s (**Figure 4a**), indicating that A-ZPO has strong hydrophilicity, which would be necessary for the rapid water adsorption. We further designed an experiment to verify whether such a rapid decrease in contact angle on the A-ZPO film is due to water adsorption or only infiltration and surface wetting effects. The schematic is shown in Figure 4b, where pure zinc phosphate powder was flattened on a glass slide to form a film, and a drop of water (~2.0 μl) was dripped on the film surface. After 5 seconds, an absorbent paper was pressed on the water spot, and the absorbent paper state (dry or wet) was observed to confirm the strong adsorption rather than pure infiltration or wetting. The results in Figure 4c show that the paper remained dry when it was pressed on the water adsorption spot of the A-ZPO film, indicating that the A-ZPO film had adsorbed the water instead of simply infiltrating and wetting the A-ZPO film. As a control, C-ZPO was also tested under the same conditions. However, the paper was wetted, suggesting that the water was incompletely adsorbed by C-ZPO and only wetting the C-ZPO film at such a short time. This finding indicated its weaker water adsorption capacity than A-ZPO. Second, the XRD results in Figure 4d show that the nature of amorphous state of A-ZPO was unchanged when the A-ZPO was placed in humid air for 12 h (A-ZPO[12h]) and 24 h (A-ZPO[24h]). In addition, 30 wt% of water was directly added into the A-ZPO (A-ZPO+H₂O[30wt%]), and the A-ZPO was re-dried with added water at 100 °C for 8 h (A-ZPO[100 °C, 8 h]). However, no new crystalline phases were detected after undergoing all treatments, indicating good structural and chemical stability of the A-ZPO. Although the crystal structure of A-ZPO did not change after absorbing water, the FTIR spectra displayed two evident vibration peaks of around 3400 and 1640 cm^{-1} belonging to the absorbed water, as shown in Figure 4e; the relative intensity of the peaks increased with the increase in the water content.^[29] The absorption of water in the prepared samples was also detected by IR when placed in the air, showing that all the prepared samples showed the vibration peaks of water (Figure S10). Third, TGA analysis also confirmed the existence of adsorbed water (Figure 4f). When A-ZPO with different degrees of adsorbed water was heated, the desorption

process of water occurred. The results showed that the temperatures of water desorption were lower than 100 °C, such a low desorption temperature indicates that the mechanism of water adsorption was physisorption without chemical reactions. This conclusion matches well with the XRD results. Undoubtedly, low desorption temperature is conducive to removing the absorbed water through redrying the electrodes. It also avoids the influence of using high temperature or residual adsorption water on the electrochemical performance of the electrodes.

In summary, the phosphorus-based electrodes are easily oxidized when exposed to moist air, and then the formed phosphorus oxides (P_xO_y) further reacting with water generate phosphoric acid or pyrophosphoric acid.^[13b, 30] At last stage, the formed pyrophosphoric acid react with copper oxide (CuO) forming copper pyrophosphate. The presence of CuO layer on the surface of Cu current collector has been confirmed by XPS results after removing the electrode materials (Figure S11). According to the above results and analysis, the main proposed reactions are as follows:



As shown in Figure 4g, in the presence of A-ZPO, although the oxidation of phosphorus-based materials was not inhibited, the water on the electrode surface can be absorbed by A-ZPO, leading to the reduction of further hydrolysis of phosphorus oxide. As a result, further deterioration of phosphorus electrode was avoided and the stability of the electrode against humid air was improved.

The electrochemical properties were analyzed for potassium-ion storage in the nonflammable TEP (triethyl phosphate) electrolyte on the basis of safety and good electrochemical stability.^[21] The safety of TEP-based electrolyte had also been confirmed by igniting BP@C@ZPO(30) electrode soaked with EC/DEC and TEP-based electrolytes

(Figure S12). The results showed a violent combustion occurred in the EC/DEC electrolyte, by contrast, the electrode was extinguished immediately after removing the open flame in TEP-based electrolyte, indicating its excellent flame-retardant property. The cyclic voltammetry (CV) curves of five electrodes were provided, as shown in **Figure 5a** and S13, at the scan rate of 0.05 mV s^{-1} in the range of $0.01\text{--}3.0 \text{ V}$ (vs K/K^+). All five electrodes showed similar CV curves in spite of the addition of A-ZPO due to the electrochemical inactivity of A-ZPO to potassium-ion (Figure S14). The two evident cathodic peaks of C_1 ($\sim 0.75 \text{ V}$) and C_2 ($\sim 0.2 \text{ V}$) correspond to the anodic peaks of A_1 ($\sim 1.6 \text{ V}$) and A_2 ($\sim 0.75 \text{ V}$), respectively.^[31] Figure 5b shows the first three galvanostatic charge/discharge voltage profiles of the BP@C@ZPO(30) electrode at the current density of 0.05 A g^{-1} , and the potentials of potassiation/depotassiation platforms are consistent with the cathodic/anodic peaks of the CV curves. The BP@C@ZPO(30) electrode showed an initial reversible charge capacity of $690.6 \text{ mA h g}^{-1}$ with corresponding initial Coulombic efficiencies (ICEs) of 69.5%. The capacity was calculated based on the total mass of phosphorus and A-ZPO, and the capacity of carbon was also provided in Figure S15, which contributed to a capacity of $\sim 45 \text{ mA h g}^{-1}$ at 0.1 A g^{-1} . In addition, the first charge/discharge capacities decreased with the increase in the A-ZPO added, and all five samples showed similar ICEs (Figure 5c). Figure 5d shows the rate performance. By contrast, the BP@C@ZPO(30) electrode presented the best rate capability and delivered the average discharge capacities of 743.9, 673.0, 620.5, 375.1, 255.4, and 229.4 mA h g^{-1} at the current densities of 0.05, 0.1, 0.2, 0.5, 1.0, and 2.0 A g^{-1} , respectively, and the capacity rebounded when the current density returned to 0.05 A g^{-1} . The long-term cycling performance at 0.5 A g^{-1} was also provided to verify the cycling stability, as shown in Figure 5e. Five cycle activation at 0.1 A g^{-1} was executed before testing at 0.5 A g^{-1} . The BP@C@ZPO(0) electrode showed the maximum initial discharge capacity of $491.9 \text{ mA h g}^{-1}$ (6th cycle) at 0.5 A g^{-1} compared with the BP@C@ZPO(30) electrode of $429.2 \text{ mA h g}^{-1}$. However, the retained capacity of the BP@C@ZPO(0) was only 15.9 mA h g^{-1} after 500

cycles, whereas the retained capacity of BP@C@ZPO(30) was 369.0 mA h g⁻¹. The increased reversible capacity of BP@C@ZPO(30) electrode before ≈50 cycles is attributed to the activation.^[20a] In addition, the BP@C@ZPO(40) electrode showed an enhanced electrochemical stability, but its reversible capacity was slightly lower than that of BP@C@ZPO(30) electrode, confirming that BP@C@ZPO(30) material has the best electrochemical performance among all five electrodes. As expected, the BP@C@ZPO(30) electrode showed poor cycling stability in the conventional EC/DEC electrolyte due to the unstable SEI, and the retaining capacity was only 267.7 mA h g⁻¹ after 100 cycles at 0.5 A g⁻¹ (Figure S16).^[21a, 32] The potassium-ion storage performance of BP@C@ZPO(30) electrode was also analyzed after exposing the electrodes to air for two days to verify the enhanced environmental stability of electrodes, as shown in Figure 5f, the BP@C@ZPO(30) electrode delivered a retained discharge capacity of 629.2 mA h g⁻¹ after 200 cycles at 0.2 A g⁻¹, which is just slightly low compared with its fresh electrode with a retained capacity of 655.0 mA h g⁻¹ after 200 cycles (Figure S17). However, the BP@C@ZPO(0) electrode showed very poor electrochemical performance in the same conditions, and the discharge capacity of only 136.7 mA h g⁻¹ was obtained after 100 cycles at 0.2 A g⁻¹ compared with the fresh BP@C@ZPO(0) electrode of 506.3 mA h g⁻¹ after 200 cycles. The results confirmed that the BP@C@ZPO(30) maintained better electrochemical performance than the BP@C@ZPO(0) when exposed to humid air. Meanwhile, the slight change on the discharge/charge curves after cycling also confirmed the stability of the BP@C@ZPO(30) electrode when exposed to air (Figure 5g). Evidently, the BP@C@ZPO(30) electrode showed an excellent high capacity and cycling stability among all the reported phosphorus anodes for PIBs (Figure 5h).

We conducted further analysis to account for the enhanced electrochemical performance when introducing A-ZPO. First, AC impedance analysis of the electrodes was conducted after 10 cycles. The charge transfer impedance (R_{ct}) decreased from 452.8 Ω of BP@C@ZPO(0) electrode to 174.7 Ω of BP@C@ZPO(30) electrode with the increase in the

A-ZPO (Figure 6a), partly explaining the improved rate capability with A-ZPO addition. Moreover, the decrease in R_{ct} can be attributed to decrease in particle size. Second, galvanostatic intermittent titration technique (GITT) was employed to analyze the K-ion diffusion coefficient of electrodes. The GITT data were collected after 10 cycles of activation. In all five electrodes, the average K-ion diffusion coefficients of depotassiation (charge) process are higher than those of potassiation (discharge) process (Figure 6b, c and S18). A rapid decline in the diffusion coefficients was observed when the potential is lower than 0.5 V during the potassiation (discharge) process in all samples; this finding can be attributed to the formation of some deep potassiation phases.^[3a] On the contrary, the BP@C@ZPO(30) electrode showed the highest average diffusion coefficients among all electrodes during the potassiation (discharge) and depotassiation (charge) processes, which can also explain the best rate performance. Third, the BP@C@ZPO(30) electrode still showed a high specific capacity despite considering the inactive A-ZPO when calculating the specific capacity. The theoretical capacity of BP@C@ZPO(30) reached $1038.4 \text{ mA h g}^{-1}$ ($2596 \text{ mA h g}^{-1} * 0.4$) when forming K_3P phase, and the K_3P (JCPDF-74-0128) phase was confirmed by the ex-situ XRD data (Figure 6d),^[3a] thereby explaining the high capacity of the BP@C@ZPO(30) electrode. In addition, some diffraction peaks belonging to $KOH \cdot H_2O$ (JCPDS No. 77-1221) were detected due to the side reactions of unstable discharge products when the electrodes discharged to 0.01V during ex-situ XRD tests. Lastly, the volume expansion rates of five electrodes were also analyzed to verify the function of the addition of A-ZPO to reduce the volume expansion. In addition, the volume expansion rate was calculated by measuring the thickness change of electrodes of fresh and after discharging (potassiation).^[5, 17] Compared with BP@C@ZPO(30) electrode, BP@C@ZPO(0) electrode showed an evident falling off of active materials from the current collector after discharging to 0.01 V (Figure S19a). Meanwhile, Figure S19b-f shows the cross-section SEM images of all five electrodes of fresh and after discharging to 0.01 V. All electrodes displayed an increase in the electrode thickness

when discharging to 0.01 V. Moreover, the calculated volume expansion rates decreased monotonically from 100% to 39.1% with the increase in A-ZPO from 0wt% to 40wt% (Figure 6e). The results confirmed the positive effects on the alleviation of volume variation when introducing the A-ZPO.

The full-cell was assembled using Prussian blue analogue (PBA, $\text{K}_2\text{FeFe}[\text{CN}]_6$) and BP@C@ZPO(30) as the cathode and anode, respectively (Figure 6f). The synthesis of $\text{K}_2\text{FeFe}(\text{CN})_6$ and its electrochemical performance for PIBs half-cell had been reported.^[17, 33] The nonflammable TEP electrolyte was selected as the electrolyte, and the voltage window of charging and discharging was from 0.5 V to 3.6 V. The full-cell showed good rate performance, delivering the average discharge capacities of 308.7, 270.9, 249.7, and 222.8 mA h g^{-1} at the current densities of 20, 50, 100, and 200 mA g^{-1} , respectively, as shown in Figure 6g and h. The retained capacity was 216.5 mA h g^{-1} after 100 cycles at 100 mA g^{-1} (Figure 6i, Figure S20). The results verify the potential of the BP@C@ZPO(30) material in practical application.

Conclusion

Amorphous BP nanocomposites were obtained by dry ball milling method when introducing A-ZPO. The addition of A-ZPO acted as a multifunctional additive. 1) The presence of A-ZPO acted as the grinding aid, which reduced the aggregation of P and improved the dispersibility, thereby increasing the utilization rate of active components. 2) The existence of A-ZPO decreased the volume expansion rates of the phosphorus electrodes due to the inactive nature. 3) The addition of A-ZPO improved the environment stability of phosphorus electrodes in humid air on the basis of the fast water adsorption capacity of the amorphous zinc phosphate. Based on above effects, the optimized BP@C@ZPO(30) electrode exhibited excellent electrochemical performance as PIB anode in TEP electrolyte. In addition, a capacity of 369.0 mA h g^{-1} was retained after 500 cycles at 0.5A g^{-1} . Meanwhile,

the capacity of 629.2 mA h g⁻¹ was obtained after 200 cycles at 0.2 A g⁻¹ in spite of the exposure to air for two days. In summary, such a low-cost and effective strategy is expected to accelerate the development and application of phosphorus as metal-ion battery anode.

Supporting Information

Supporting Information is available from the Wiley Online Library or from the author.

Acknowledgements

This work was funded by the Science and Technology Development Fund, Macau SAR (File no. 0191/2017/A3, 0041/2019/A1, 0046/2019/AFJ, 0021/2019/AIR), University of Macau (File no. MYRG2017-00216-FST and MYRG2018-00192-IAPME) and the UEA funding.

Conflict of Interest

The authors declare no conflict of interest.

Credit Author Statement

Shunping Ji: Conceptualization, Data Curation, Formal Analysis, Investigation, Methodology, Writing, Original Draft, Writing, Review & Editing

Yunshan Zheng: Data Curation, Formal Analysis, Writing,

Kwan San Hui: Conceptualization, Supervision, Writing, Review & Editing

Junfeng Li: Data Curation, Formal Analysis

Kaixi Wang: Data Curation, Formal Analysis

Chunyan Song: Data Curation, Formal Analysis

Huifang Xu: Writing, Original Draft, Writing, Review & Editing

Shuo Wang: Writing, Original Draft, Writing, Review & Editing

Chenyang Zha: Materials preparation, Writing – Review & Editing

Duc Anh Dinh: Data Curation

Zikang Tang: Investigation, Methodology, Writing, Review & Editing

Zongping Shao: Conceptualization, Supervision, Writing, Review & Editing

Kwun Nam Hui: Conceptualization, Supervision, Writing, Review & Editing

Declaration of interests

☒ The authors declare that they have no known competing financial interests or personal relationships that could have appeared to influence the work reported in this paper.

References

- [1] a) T. Hosaka, K. Kubota, A. S. Hameed, S. Komaba, *Chem. Rev.* **2020**, 120, 6358; b) S. Dhir, S. Wheeler, I. Capone, M. Pasta, *Chem* **2020**, 6, 2442; c) X. Min, J. Xiao, M. H. Fang, W. Wang, Y. J. Zhao, Y. G. Liu, A. M. Abdelkader, K. Xi, R. V. Kumar, Z. H. Huang, *Energy Environ. Sci.* **2021**, 14, 2186.
- [2] a) J. Zhao, X. Zou, Y. Zhu, Y. Xu, C. Wang, *Adv. Funct. Mater.* **2016**, 26, 8103; b) L. Fan, R. Ma, Q. Zhang, X. Jia, B. Lu, *Angew. Chem. Int. Ed.* **2019**, 58, 10500.
- [3] a) H. Jin, H. Wang, Z. Qi, D. S. Bin, T. Zhang, Y. Wan, J. Chen, C. Chuang, Y. R. Lu, T. S. Chan, H. Ju, A. M. Cao, W. Yan, X. Wu, H. Ji, L. J. Wan, *Angew. Chem. Int. Ed.* **2020**, 59, 2318; b) W. C. Chang, J. H. Wu, K. T. Chen, H. Y. Tuan, *Adv. Sci.* **2019**, 6, 1801354; c) T. Xu, D. Li, S. Chen, Y. Sun, H. Zhang, Y. Xia, D. Yang, *Chem. Eng. J.* **2018**, 345, 604; d) Y. Wu, H. B. Huang, Y. Feng, Z. S. Wu, Y. Yu, *Adv. Mater.* **2019**, 31, 1901414; e) X. L. Huang, F. Zhao, Y. Qi, Y.-A. Qiu, J. S. Chen, H. K. Liu, S. X. Dou, Z. M. Wang, *Energy Storage Mater.* **2021**, 42, 193; f) J. H. Zhou, Q. T. Shi, S. Ullah, X. Q. Yang, A. Bachmatiuk, R. Z. Yang, M. H. Rummeli, *Adv. Funct. Mater.* **2020**, 30, 2004648.
- [4] Y. Wu, S. Hu, R. Xu, J. Wang, Z. Peng, Q. Zhang, Y. Yu, *Nano Lett.* **2019**, 19, 1351.
- [5] P. Xiong, P. Bai, S. Tu, M. Cheng, J. Zhang, J. Sun, Y. Xu, *Small* **2018**, 14, 1802140.
- [6] a) J. Sun, G. Zheng, H. W. Lee, N. Liu, H. Wang, H. Yao, W. Yang, Y. Cui, *Nano Lett.* **2014**, 14, 4573; b) D. Liu, X. Huang, D. Qu, D. Zheng, G. Wang, J. Harris, J. Si, T. Ding, J. Chen, D. Qu, *Nano Energy* **2018**, 52, 1; c) J. Zhou, X. Liu, L. Zhu, S. Niu, J. Cai, X. Zheng, J. Ye, Y. Lin, L. Zheng, Z. Zhu, D. Sun, Z. Lu, Y. Zang, Y. Wu, J. Xiao, Q. Liu, Y. Zhu, G. Wang, Y. Qian, *Chem* **2020**, 6, 221.
- [7] a) S. H. Choi, G. Nam, S. Chae, D. Kim, N. Kim, W. S. Kim, J. Ma, J. Sung, S. M. Han, M. Ko, H. W. Lee, J. Cho, *Adv. Energy Mater.* **2019**, 9, 1803121; b) J. Chen, X. Fan, Q. Li, H. Yang, M. R. Khoshi, Y. Xu, S. Hwang, L. Chen, X. Ji, C. Yang, H. He, C. Wang, E. Garfunkel, D. Su, O. Borodin, C. Wang, *Nat. Energy* **2020**, 5, 386.
- [8] a) U. Kasavajjula, C. Wang, A. J. Appleby, *J. Power Sources* **2007**, 163, 1003; b) P. G. Bruce, B. Scrosati, J. M. Tarascon, *Angew. Chem. Int. Ed.* **2008**, 47, 2930; c) Y. Liu, Z. Tai, J. Zhang, W. K. Pang, Q. Zhang, H. Feng, K. Konstantinov, Z. Guo, H. K. Liu, *Nat. Commun.* **2018**, 9, 1.
- [9] D. Su, J. Dai, M. Yang, J. Wen, J. Yang, W. Liu, H. Hu, L. Liu, Y. Feng, *Nanoscale* **2021**, 13, 6635.
- [10] X. Sui, X. Huang, H. Pu, Y. Wang, J. Chen, *Nano Energy* **2021**, 83, 105797.
- [11] a) G. Ma, K. Huang, J.-S. Ma, Z. Ju, Z. Xing, Q.-c. Zhuang, *J. Mater. Chem. A* **2017**, 5, 7854; b) H. Wang, L. Wang, L. Wang, Z. Xing, X. Wu, W. Zhao, X. Qi, Z. Ju, Q. Zhuang, *Chem. Eur. J.* **2018**, 24, 13897; c) J. Ruan, F. Mo, Z. Long, Y. Song, F. Fang, D. Sun, S. Zheng, *ACS nano* **2020**, 14, 12222.
- [12] G. Qin, Y. Liu, F. Liu, X. Sun, L. Hou, B. Liu, C. Yuan, *Adv. Energy Mater.* **2020**, DOI: 10.1002/aenm.2020034292003429.
- [13] a) Y. Zhang, C. Ma, J. Xie, H. Agren, H. Zhang, *Adv. Mater.* **2021**, 33, 2100113; b) T. Zhang, Y. Wan, H. Xie, Y. Mu, P. Du, D. Wang, X. Wu, H. Ji, L. Wan, *J. Am. Chem. Soc.* **2018**, 140, 7561; c) Y. Zhao, H. Wang, H. Huang, Q. Xiao, Y. Xu, Z. Guo, H. Xie, J. Shao, Z. Sun, W. Han, X. F. Yu, P. Li, P. K. Chu, *Angew. Chem. Int. Ed.* **2016**, 55,

5003.

- [14] K. Fang, D. Liu, X. Xiang, X. Zhu, H. Tang, D. Qu, Z. Xie, J. Li, D. Qu, *Nano Energy* **2020**, 69, 104451.
- [15] a) D. Peng, Y. Chen, H. Ma, L. Zhang, Y. Hu, X. Chen, Y. Cui, Y. Shi, Q. Zhuang, Z. Ju, *ACS Appl. Mater. Interfaces* **2020**, 12, 37275; b) I. Capone, J. Aspinall, H. J. Lee, A. W. Xiao, J. Ihli, M. Pasta, *Mater. Today Energy* **2021**, 21, 100840; c) X. Wu, W. Zhao, H. Wang, X. Qi, Z. Xing, Q. Zhuang, Z. Ju, *J. Power Sources* **2018**, 378, 460.
- [16] Z. Wei, D. Wang, X. Yang, C. Wang, G. Chen, F. Du, *Adv. Mater. Interfaces* **2018**, 5, 1800639.
- [17] S. Ji, C. Song, J. Li, K. S. Hui, W. Deng, S. Wang, H. Li, D. A. Dinh, X. Fan, S. Wu, J. Zhang, F. Chen, Z. Shao, K. N. Hui, *Adv. Energy Mater.* **2021**, 11, 2101413.
- [18] a) Z. Zhang, Y. Han, J. Xu, J. Ma, X. Zhou, J. Bao, *ACS Appl. Energy Mater.* **2018**, 1, 4395; b) F. Mattelaer, K. Geryl, G. Rampelberg, J. Dendooven, C. Detavernier, *ACS Appl. Mater. Interfaces* **2017**, 9, 13121; c) X. Yang, R.-Y. Zhang, J. Zhao, Z.-X. Wei, D.-X. Wang, X.-F. Bie, Y. Gao, J. Wang, F. Du, G. Chen, *Adv. Energy Mater.* **2018**, 8, 1701827; d) S. Zhou, Z. Tao, J. Liu, X. Wang, T. Mei, X. Wang, *ACS Omega* **2019**, 4, 6452; e) J. S. Thorne, R. A. Dunlap, M. N. Obrovac, *Electrochim. Acta* **2013**, 112, 133; f) X. Xu, C. Niu, M. Duan, X. Wang, L. Huang, J. Wang, L. Pu, W. Ren, C. Shi, J. Meng, B. Song, L. Mai, *Nat. Commun.* **2017**, 8, 460.
- [19] S. Bach, V. R. Celinski, M. Dietzsch, M. Panthofer, R. Bienert, F. Emmerling, J. Schmedt auf der Gunne, W. Tremel, *J. Am. Chem. Soc.* **2015**, 137, 2285.
- [20] a) H. Wang, D. Yu, X. Wang, Z. Niu, M. Chen, L. Cheng, W. Zhou, L. Guo, *Angew. Chem. Int. Ed.* **2019**, 58, 16451; b) X. Du, B. Zhang, *ACS nano* **2021**, 15, 16851; c) J. Zhang, Z. Cao, L. Zhou, G.-T. Park, L. Cavallo, L. Wang, H. N. Alshareef, Y.-K. Sun, J. Ming, *ACS Energy Lett.* **2020**, DOI: 10.1021/acseenergylett.0c01634; d) L. Zhou, Z. Cao, J. Zhang, H. Cheng, G. Liu, G. T. Park, L. Cavallo, L. Wang, H. N. Alshareef, Y. K. Sun, J. Ming, *Adv. Mater.* **2021**, 33, 2005993.
- [21] a) S. Liu, J. Mao, Q. Zhang, Z. Wang, W. K. Pang, L. Zhang, A. Du, V. Sencadas, W. Zhang, Z. Guo, *Angew. Chem. Int. Ed.* **2020**, 59, 3638; b) L. Deng, T. Wang, Y. Hong, M. Feng, R. Wang, J. Zhang, Q. Zhang, J. Wang, L. Zeng, Y. Zhu, L. Guo, *ACS Energy Lett.* **2020**, 5, 1916.
- [22] C. M. Park, H. J. Sohn, *Adv. Mater.* **2007**, 19, 2465.
- [23] a) G. Hu, T. Albrow-Owen, X. Jin, A. Ali, Y. Hu, R. C. T. Howe, K. Shehzad, Z. Yang, X. Zhu, R. I. Woodward, T. C. Wu, H. Jussila, J. B. Wu, P. Peng, P. H. Tan, Z. Sun, E. J. R. Kelleher, M. Zhang, Y. Xu, T. Hasan, *Nat. Commun.* **2017**, 8, 278; b) P. Nakhnivej, X. Yu, S. K. Park, S. Kim, J. Y. Hong, H. J. Kim, W. Lee, J. Y. Hwang, J. E. Yang, C. Wolverton, J. Kong, M. Chhowalla, H. S. Park, *Nat. Mater.* **2019**, 18, 156.
- [24] J. Yang, Z. Ju, Y. Jiang, Z. Xing, B. Xi, J. Feng, S. Xiong, *Adv. Mater.* **2018**, 30, 1700104.
- [25] a) L. Tao, Y. Yang, H. Wang, Y. Zheng, H. Hao, W. Song, J. Shi, M. Huang, D. Mitlin, *Energy Storage Mater.* **2020**, 27, 212; b) D. P. Qiu, J. Y. Guan, M. Li, C. H. Kang, J. Y. Wei, Y. Li, Z. Y. Xie, F. Wang, R. Yang, *Adv. Funct. Mater.* **2019**, 29, 1903496; c) T. Zhang, D. Qiu, Y. Hou, *Nano Energy* **2022**, 94, 106909.
- [26] A. Chhetry, S. Sharma, S. C. Barman, H. Yoon, S. Ko, C. Park, S. Yoon, H. Kim, J. Y. Park, *Adv. Funct. Mater.* **2020**, 31, 2007661.
- [27] a) N. Blanc, C. Mayer-Laigle, X. Frank, F. Radjai, J. Y. Delenne, *Powder Technol.* **2020**, 376, 661; b) P. L. Guzzo, F. B. M. de Barros, B. R. Soares, J. B. Santos, *Powder Technol.* **2020**, 368, 149.
- [28] a) G. Zhang, C. E. Shaffer, C.-Y. Wang, C. D. Rahn, *J. Electrochem. Soc.* **2013**, 160, A2299; b) M. M. Forouzan, B. A. Mazzeo, D. R. Wheeler, *J. Electrochem. Soc.* **2018**, 165, A2127; c) J. Li, N. Sharma, Z. Jiang, Y. Yang, F. Monaco, Z. Xu, D. Hou, D. Ratner, P. Pianetta, P. Cloetens, F. Lin, K. Zhao, Y. Liu, *Science* **2022**, 376, 517.

- [29] S. P. Ji, M. Tang, L. He, G. H. Tao, *Chem. Eur. J.* **2013**, 19, 4452.
- [30] C. Marino, M. El Kazzi, E. J. Berg, M. He, C. Villeveille, *Chem. Mater.* **2017**, 29, 7151.
- [31] I. Sultana, M. M. Rahman, T. Ramireddy, Y. Chen, A. M. Glushenkov, *J. Mater. Chem. A* **2017**, 5, 23506.
- [32] B. Li, J. Zhao, Z. Zhang, C. Zhao, P. Sun, P. Bai, J. Yang, Z. Zhou, Y. Xu, *Adv. Funct. Mater.* **2019**, 20, 1807137.
- [33] C. Li, X. Wang, W. Deng, C. Liu, J. Chen, R. Li, M. Xue, *ChemElectroChem* **2018**, 5, 3887.

Figures and captions:

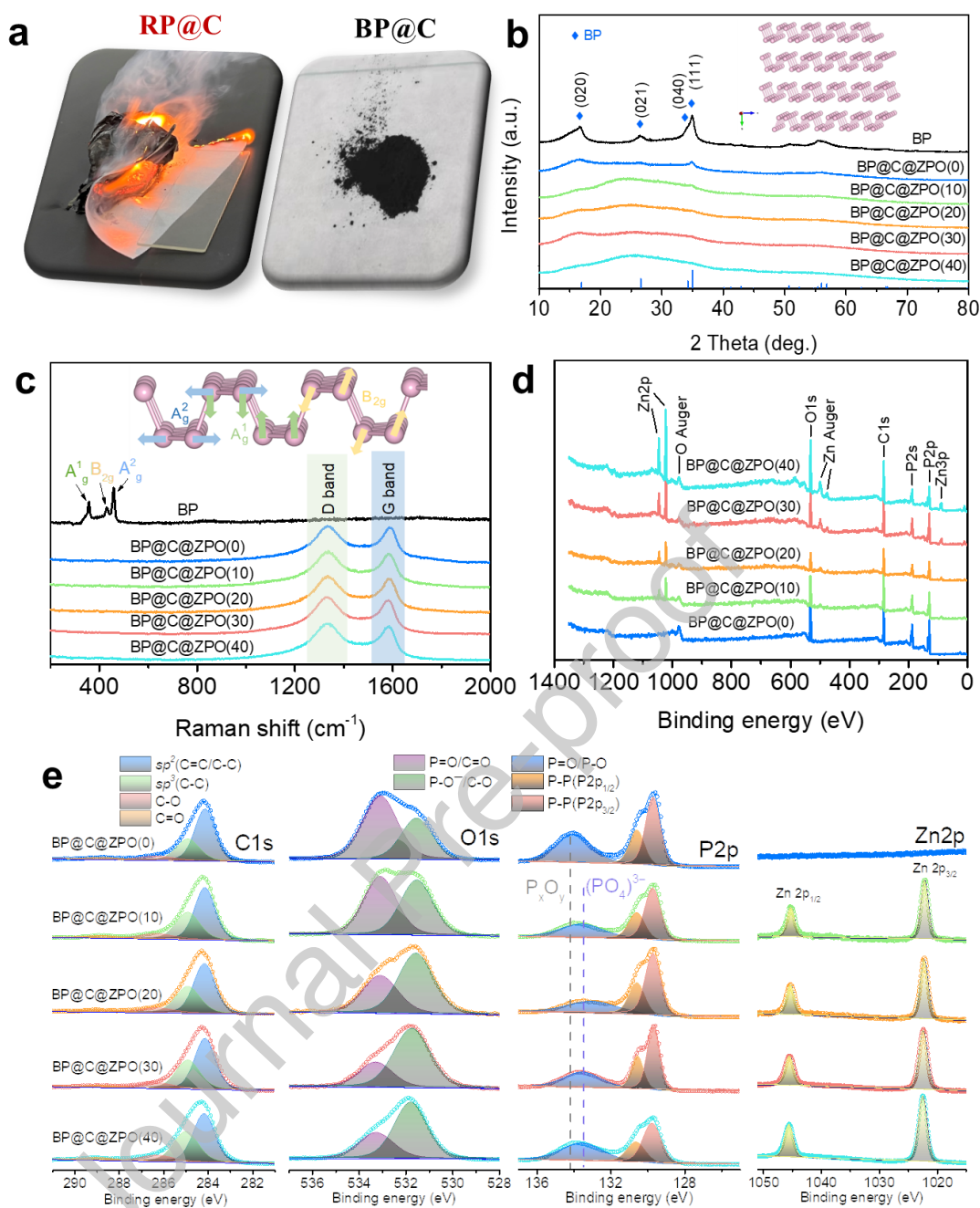


Figure 1. a) Digital images of RP@C and BP@C composites when exposed to air after preparing by dry ball milling method. b) XRD patterns of BP and BP composites with different mass ratio of A-ZPO (inset: crystal structure of BP). c) Raman spectra. d) XPS survey spectra. e) High-resolution XPS spectra of C 1s, O 1s, P 2p, and Zn 2p elements.

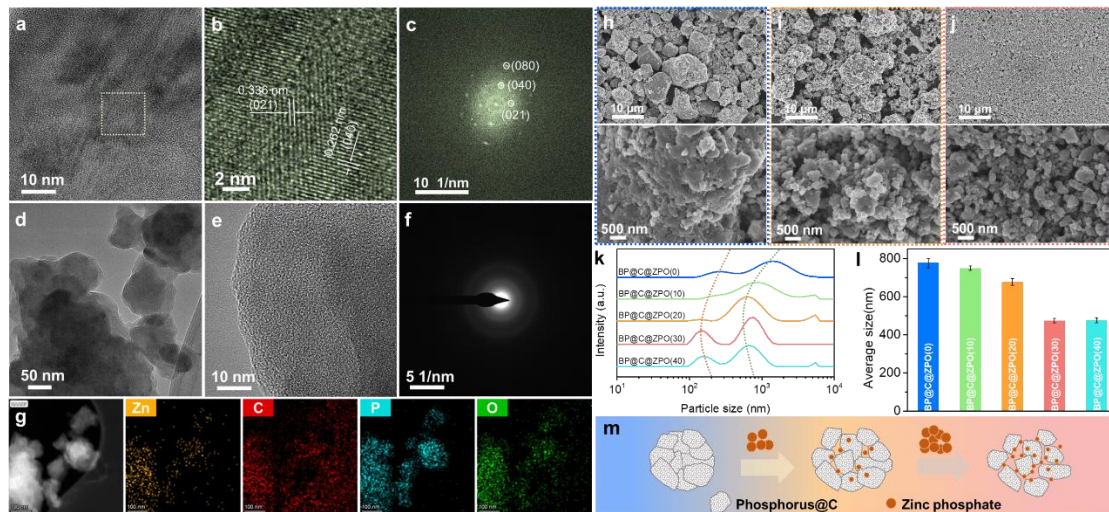


Figure 2. a) HRTEM image of pure BP. b) HRTEM image recorded from the area marked with green box in (a) and (c) corresponding FFT pattern. d) TEM image and e) HRTEM image of BP@C@ZPO(30). f) SAED pattern of BP@C@ZPO(30). g) Dark-field TEM image and Zn, C, P, and O elemental maps of BP@C@ZPO(30). SEM images of h) BP@C@ZPO(0), i) BP@C@ZPO(20), and j) BP@C@ZPO(30). k) Particle size distribution of prepared samples by using dynamic light scattering measurement. l) Comparison of the average size of prepared samples. m) Schematic of grinding aid effect of zinc phosphate.

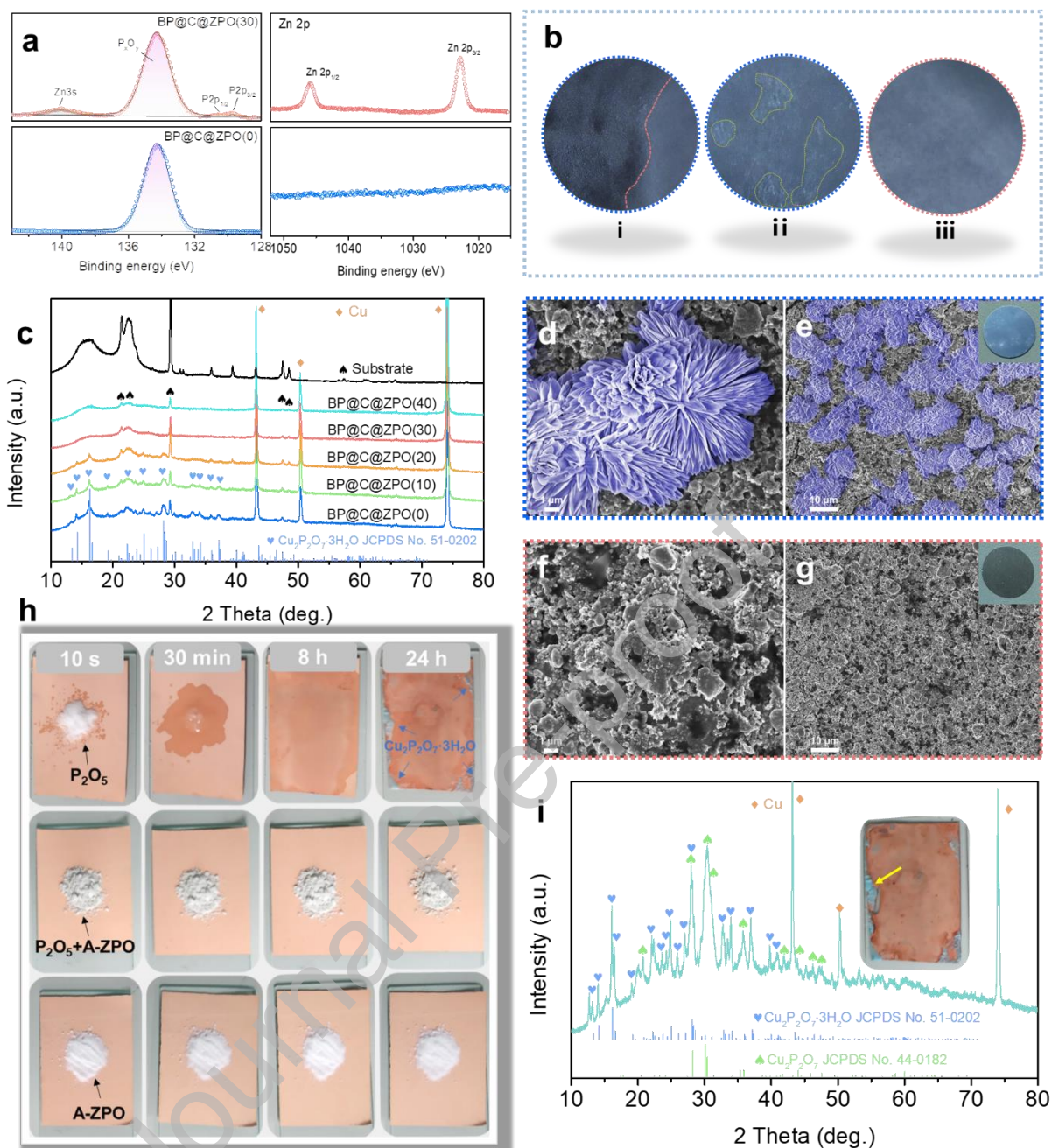


Figure 3. a) High-resolution P2p and Zn2p spectra of BP@C@ZPO(0) and BP@C@ZPO(30) samples after placing in air for three days. b) Digital images of (i) BP@C@ZPO(0) electrode exposed to moisture air, (ii) re-drying the BP@C@ZPO(0), and (iii) BP@C@ZPO(30) electrode exposed to moisture air. c) XRD patterns of electrodes after exposing to moisture air for three days. SEM images of (d, e) BP@C@ZPO(0) and (f, g) BP@C@ZPO(30) electrodes after exposing to moisture air for three days. The insets are the digital images corresponding to electrodes. h) Digital images of pure P_2O_5 , a mixture of P_2O_5 and A-ZPO (mass ratio:

$P_2O_5/A-ZPO = 3/7$), and pure A-ZPO were placed on the copper foils and exposed to moisture air for different times. (i) XRD pattern of the copper foil after placing pure P_2O_5 for 24 h.

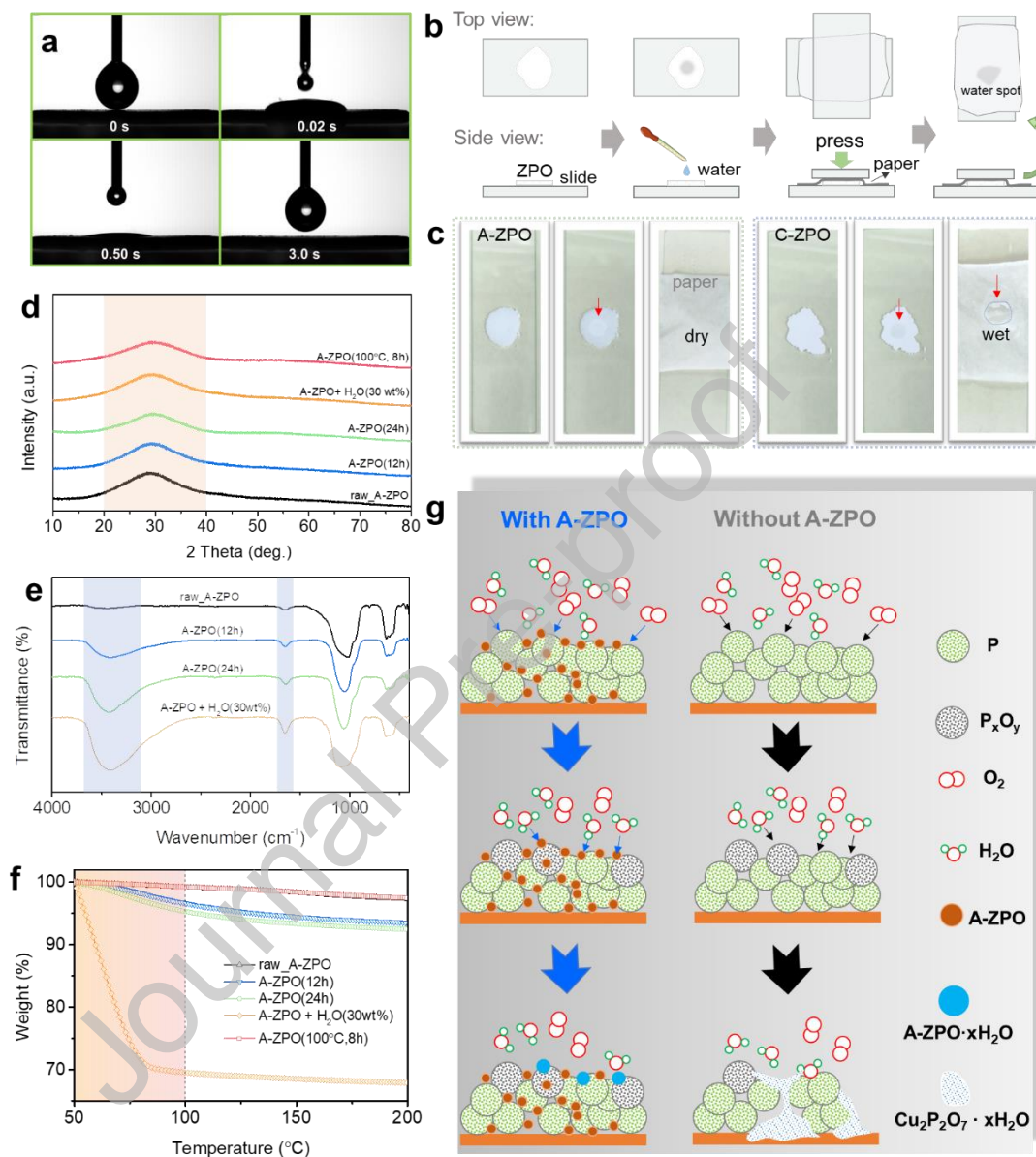


Figure 4. a) Contact angles of pure A-ZPO. b) Schematic process to verify the fast water absorption of ZPO and c) corresponding digital images of A-ZPO and C-ZPO samples. d) XRD patterns of A-ZPO after different treatments. e) IR spectra. f) TG analysis. g) Illustration of enhanced anti-moisture of the electrode with A-ZPO.

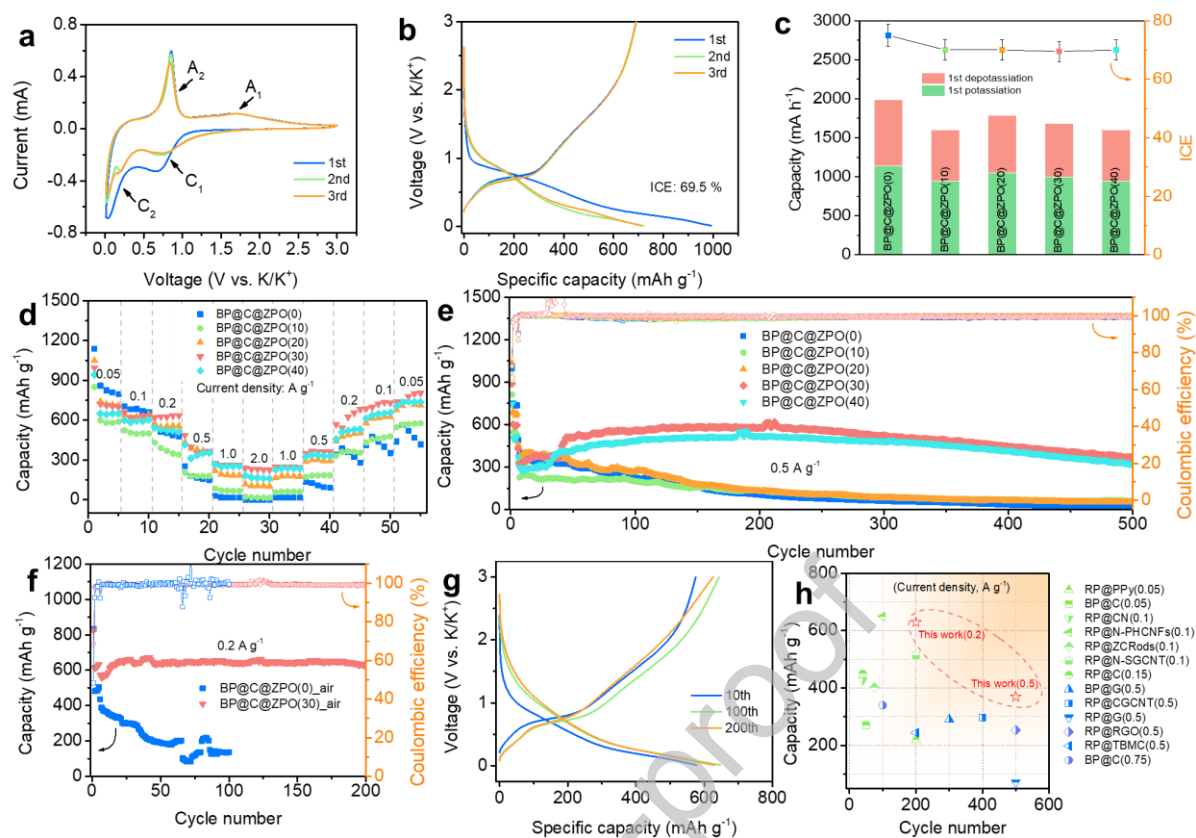


Figure 5. a) CV curves of the BP@C@ZPO(30) electrode at the scan rate of 0.05 mV s^{-1} . b) Galvanostatic charge/discharge curves of the first three cycles at 0.05 A g^{-1} for BP@C@ZPO(30) electrode. c) Comparison of the first charge/discharge capacity and the ICE of five electrodes. d) Rate performance. e) Long-term cycling stability at 0.5 A g^{-1} . f) Cycling stability and g) corresponding galvanostatic charge/discharge curves at different cycles for the BP@C@ZPO(30) electrode at 0.2 A g^{-1} after exposing the electrodes to humid air for two days. h) Comparison of cycling performance with all the reported BP and RP materials for PIB anodes, including RP@PPy(0.05),^[14] BP@C(0.05),^[31] RP@CN(0.1),^[5] RP@N-PHCNFs(0.1),^[4] RP@ZCRods(0.1),^[10] RP@N-SGCNT(0.1),^[11c] RP@C(0.15),^[3b] BP@G(0.5),^[20b] RP@CGCNT(0.5),^[15a] RP@G(0.5),^[15c] RP@RGO(0.5),^[11b] RP@TBMC(0.5),^[6b] and BP@C(0.75),^[3a] the numbers in the brackets are the current densities (A g^{-1}).

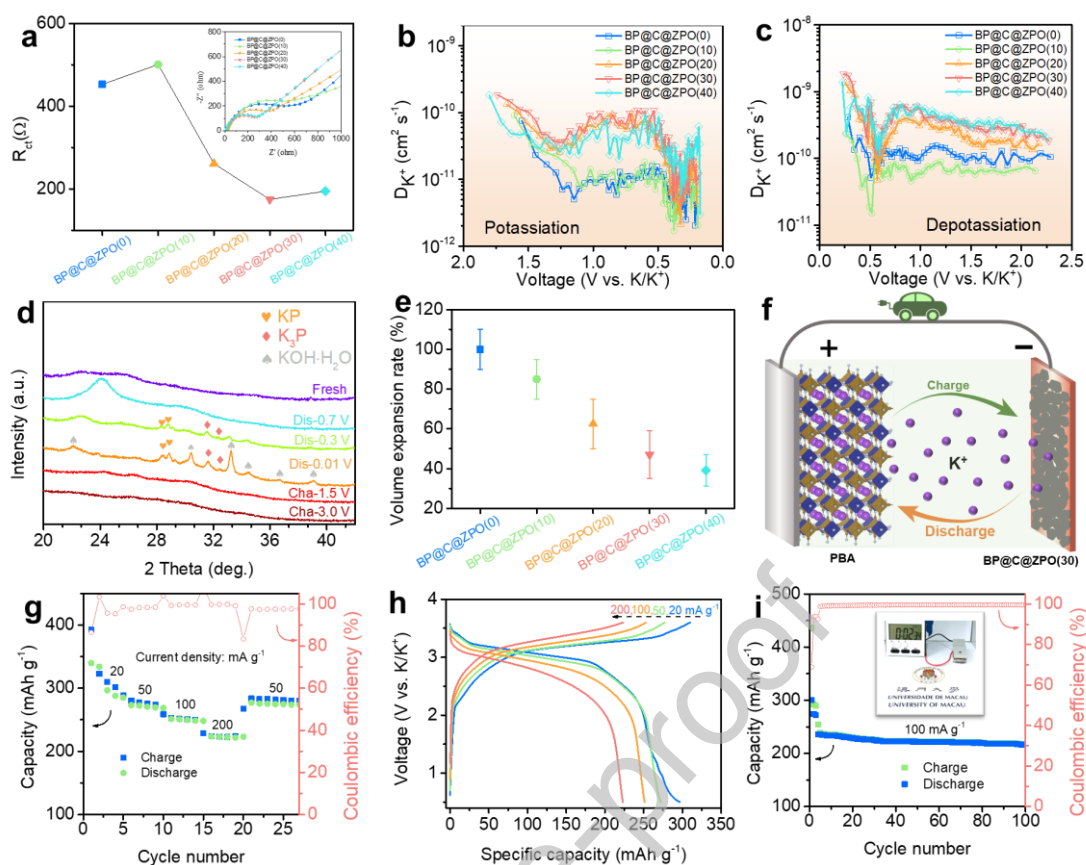


Figure 6. a) Comparison of charge transfer resistance (R_{ct}) of five electrodes after 10 cycles at 0.1 A g^{-1} in K-ion half cells. Inset is the EIS plots. b, c) Comparison of K-ion diffusion coefficient during the potassiation (discharge)/depotassiation (charge) processes after 10 cycles of activation. d) Ex-situ XRD patterns of BP@C@ZPO(30) electrodes after discharging/charging to different states. e) Calculated volume expansion rates on the basis of the thickness change of electrodes. f) Schematic of the full-cell using PBA and BP@C@ZPO(30) as the cathode and anode, respectively. g) Rate performance of the full-cell ($20\text{--}200 \text{ mA g}^{-1}$). h) Charge/discharge profiles of the full-cell at different current densities. i) Cycling performance of the full-cell at 100 mA g^{-1} . The inset displays a timer powered by the full-cell.